

Perfecting Depth: Uncertainty-Aware Enhancement of Metric Depth

Jinyoung Jun^{1,2*} Lei Chu² Jiahao Li² Yan Lu² Chang-Su Kim¹

¹Korea University ²Microsoft Research Asia

jyjun@mcl.korea.ac.kr {leichu, jiahali, yanlu}@microsoft.com changsukim@korea.ac.kr

Abstract

We propose a novel two-stage framework for sensor depth enhancement, called *Perfecting Depth*. This framework leverages the stochastic nature of diffusion models to automatically detect unreliable depth regions while preserving geometric cues. In the first stage (*stochastic estimation*), the method identifies unreliable measurements and infers geometric structure by leveraging a training–inference domain gap. In the second stage (*deterministic refinement*), it enforces structural consistency and pixel-level accuracy using the uncertainty map derived from the first stage. By combining stochastic uncertainty modeling with deterministic refinement, our method yields dense, artifact-free depth maps with improved reliability. Experimental results demonstrate its effectiveness across diverse real-world scenarios. Furthermore, theoretical analysis, various experiments, and qualitative visualizations validate its robustness and scalability. Our framework sets a new baseline for sensor depth enhancement, with potential applications in autonomous driving, robotics, and immersive technologies.

1. Introduction

Depth maps represent pixel-wise distances from scene points to the camera, providing a fundamental representation of 3D structure. They play a crucial role in various 3D tasks, such as 2D-to-3D conversion [62], 3D model generation [28], and augmented reality [18]. With the increasing availability of depth-capturing devices, dense and accurate depth maps have become essential in fields like autonomous driving, robotics, and immersive technologies.

Following breakthroughs in deep learning, monocular depth estimation has emerged as a practical alternative when depth sensors are unavailable. Early approaches focused on metric depth estimation [5, 19, 21, 37, 38]. However, they rely on specific camera datasets [24, 55], which limits real-world applicability due to scale ambiguity. To address this issue, recent research has shifted to relative

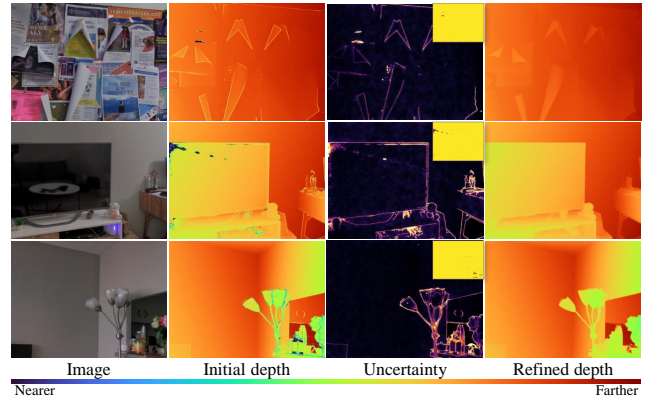


Figure 1. Sensor depth enhancement result on DIODE-Indoor. Without hand-crafted priors for noise or artifacts, our method effectively removes unreliable pixels and improves overall depth quality. Top-right inset indicates zero values in initial depth.

depth estimation, which predicts pixel-wise depth order rather than absolute values [22, 31, 49, 64].

While sufficient for some tasks, relative depth remains inadequate for applications requiring precise metric depth, such as high-fidelity 3D reconstruction or safety-critical robotic navigation. Moreover, sensor-based depth still faces challenges from hardware and environmental factors, leading to noise, missing data, and distortions—especially on reflective or transparent surfaces, as illustrated in Fig. 1. These limitations hinder the reliability of depth maps in critical applications, necessitating more advanced approaches for depth enhancement.

To address the challenges of sensor depth enhancement, we propose a general framework, *Perfecting Depth*. The key innovation of our approach lies in leveraging diffusion models to *automatically* assess the reliability of each pixel through a carefully designed training–inference gap, thereby eliminating the reliance on manually defined artifact priors. Specifically, our framework consists of a two-stage pipeline: (1) *Stochastic estimation* stage: We employ a diffusion-based strategy that trains the diffusion model on clean data but performs inference on raw, real-world data. This deliberate training–inference gap enables the model to measure per-pixel uncertainty and geometric cues, effec-

*Work done during internship at Microsoft Research Asia.

tively identifying unreliable pixels without requiring handcrafted priors. (2) *Deterministic refinement* stage: A refinement network is then applied to focus on uncertain regions, ensuring accurate corrections while preserving valid sensor measurements. By integrating the complementary strengths of stochastic sampling for global uncertainty estimation and precise local refinement for targeted corrections, our pipeline generates dense and high-quality depth maps that are well-suited for real-world tasks demanding accurate metric depth. We validate the effectiveness of our framework through theoretical analysis, extensive experiments, and qualitative visualizations, all of which demonstrate its superior performance.

Notably, the proposed framework is trained solely on synthetic data, yet it generalizes well to diverse real-world scenarios by inferring a global depth range from sensor input rather than relying on scale assumptions made during training. This underscores its potential for scalability across various real-world sensor datasets.

This paper has the following contributions:

- We introduce a novel diffusion-deterministic pipeline for sensor depth enhancement, leveraging multiple reconstructions to detect noise without handcrafted priors.
- The proposed framework provides robust generalization to unseen, real-world sensor data even with synthetic-only training.
- The proposed framework excels in various scenarios, including sensor noise removal and depth completion with noisy measurements, surpassing state-of-the-art methods in real-world scenarios.

2. Related Work

2.1. Sensor depth enhancement

Depth maps from hardware sensors often suffer from imperfections due to sensor limitations. Various approaches have been explored to effectively leverage sensor-derived depth, including depth completion, which reconstructs dense depth from sparse measurements [8, 9, 41, 44, 45, 61, 66, 70], and depth super-resolution, which enhances low-resolution depth maps for better integration with high-resolution RGB data [26, 42, 72, 73].

However, these methods often assume that input depth maps are clean. While some depth completion methods address sparsity [12, 30, 46], handling real-world noise and inaccuracies remains a challenge. Similarly, depth super-resolution can amplify artifacts, especially in regions with complex geometries or sharp depth transitions.

2.2. Diffusion models

Denoising Diffusion Probabilistic Model (DDPM) [27] is a type of generative model which progressively removes Gaussian noise to approximate specific data distributions.

Building on its superior training stability and generation quality, subsequent studies have focused on improving computational efficiency with Denoising Diffusion Implicit Model (DDIM) [56] and enabling high-resolution generation with Latent Diffusion Model (LDM) [51]. These advancements have significantly expanded the applicability of diffusion models across diverse fields, including image and video synthesis [6, 16, 20] and 3D generation [1, 67].

2.3. Diffusion models with depth

Diffusion models have been increasingly applied to depth-related tasks, primarily in monocular depth estimation [22, 29, 31, 47, 52, 57, 71], where depth maps serve as noise while image representations provide conditioning [29, 31, 52]. Another approach regenerates diverse images from a single depth map to address transparency and weather effects [57].

Conversely, using depth maps to condition RGB generation has also been explored [40, 43, 68, 69], leveraging depth for structural guidance. However, these methods often struggle with precise alignment due to the stochastic nature of diffusion models.

In contrast, our framework integrates stochastic sampling with deterministic refinement. We first generate multiple depth reconstructions using a diffusion-based masked autoencoder, then filter out unreliable pixels via multi-sample variance. The remaining reliable regions undergo deterministic refinement, ensuring structural consistency while enhancing depth with uncertainty awareness.

2.4. Masked autoencoders

Masked Autoencoders (MAEs), inspired by masked language models [15] and applied in vision transformers [17], have proven effective for self-supervised learning and image reconstruction [25, 63]. MAEs are trained by masking parts of the input and predicting the missing regions, but they rely on fixed latent representations and feedforward architectures, making their outputs deterministic.

Our work extends MAEs by integrating RGB-D input for robust depth reconstruction. During training, the depth map is partially masked and reconstructed using RGB cues. We further incorporate diffusion models to inject random noise during reconstruction, allowing us to detect unreliable regions through increased variability across multiple reconstructions. This fusion of MAEs' structured encoding with the generative flexibility of diffusion models enables both unreliable region detection and inpainting for sensor depth enhancement under real-world conditions.

2.5. Uncertainty in Neural Networks

Uncertainty in neural networks is typically divided into epistemic uncertainty, reflecting model confidence in under-represented regions, and aleatoric uncertainty, representing

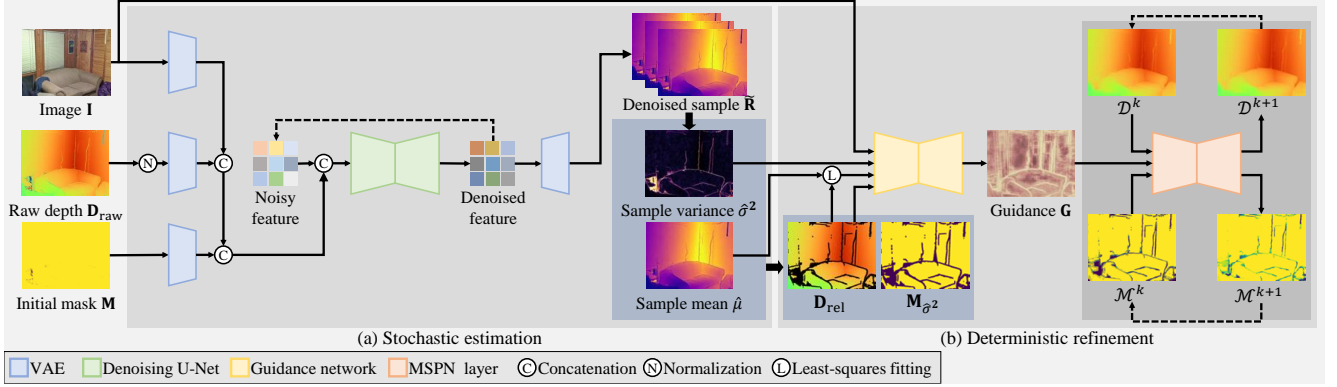


Figure 2. An overview of the proposed framework.

inherent data noise. Early works used Bayesian approximations [23, 32, 34] and ensembles [2–4, 10, 11, 14, 36, 48] to capture epistemic uncertainty. Our approach, similar to concurrent work [54], generates an ensemble through multiple denoising iterations of a single diffusion model, rather than by training multiple models. Different with these methods, the epistemic uncertainty of our pipeline is deliberately-introduced by the training–inference gap to approximate the aleatoric uncertainty observed in real-world data, such as sensor artifacts or observational ambiguities.

3. Method

Given an RGB image $\mathbf{I} \in \mathbb{R}^{3 \times H \times W}$ and its corresponding raw depth map $\mathbf{D}_{\text{raw}} \in \mathbb{R}^{H \times W}$, our goal is to estimate a dense, artifact-free refined depth map $\mathbf{D}_{\text{refine}}$ that accurately approximates the unknown ground-truth depth \mathbf{D}_{true} . However, due to hardware limitations or external factors (e.g., reflections, sensor defects), certain pixels in \mathbf{D}_{raw} become unreliable. Formally, we write:

$$\mathbf{D}_{\text{raw}} = \mathbf{D}_{\text{true}} + \mathbf{N}_{\text{sensor}}, \quad (1)$$

where $\mathbf{N}_{\text{sensor}}$ denotes a set of localized sensor artifacts that do not follow a predefined distribution (e.g., Gaussian). This assumption reflects real-world scenarios where most depth values are accurate, but specific local regions may suffer severe corruption.

As illustrated in Fig. 2, our approach consists of two main stages. In Sec. 3.1, we introduce our novel approach that leverages the stochastic properties of the diffusion process to estimate the pixel-wise uncertainty and geometric cues via a carefully designed training–inference domain gap. In Sec. 3.2, we employ a deterministic network to refine high-uncertainty regions while preserving reliable measurements. This ensures that the final depth map is globally consistent and robust to input artifacts.

3.1. Stochastic estimation

To avoid the need for manually defining the artifact prior and to enable automatic pixel-wise uncertainty estimation,

we leverage the stochastic properties of the diffusion process. Specifically, we train a diffusion probabilistic model Θ to model the conditional distribution p_{Θ} as follows:

$$p_{\Theta}(\mathbf{D}_{\text{true}} | \mathbf{I}, \mathbf{D}_{\text{cond}}, \mathbf{M}), \quad (2)$$

where \mathbf{M} is a random mask and $\mathbf{D}_{\text{cond}} \triangleq \mathbf{M} \otimes \mathbf{D}_{\text{true}}$ during training (\otimes represents the Hadamard product). Rather than enumerating various types of artifacts during training, we train the diffusion network exclusively on clean data. Moreover, to prevent the model from overfitting to the metric range of the training data, we also apply scale-shift normalization that maps the depth values to the range $[-1, 1]$.

During inference, we condition the diffusion process on the raw depth map by setting $\mathbf{D}_{\text{cond}} = \mathbf{D}_{\text{raw}}$, where \mathbf{M} denotes the valid mask of non-zero values in \mathbf{D}_{raw} . We will later show that this training–inference gap is key to estimating pixel reliability. We perform the denoising process N times, starting from different random noise realizations, and obtain a set of denoised samples $\{\tilde{\mathbf{R}}_i\}_{i=1}^N$. The pixel-wise expectation and variance of these samples are then utilized as both the geometric cues and uncertainty indicators for \mathbf{D}_{raw} , respectively. Formally:

$$\tilde{\mathbf{R}} \sim p_{\Theta}(\mathbf{D}_{\text{true}} | \mathbf{I}, \mathbf{D}_{\text{cond}}, \mathbf{M}). \quad (3)$$

The pixel-wise posterior mean and variance are given by:

$$\mu(x, y) = \mathbb{E}_{p_{\Theta}}[\tilde{\mathbf{R}}(x, y)], \quad \sigma^2(x, y) = \text{Var}_{p_{\Theta}}[\tilde{\mathbf{R}}(x, y)]. \quad (4)$$

And we approximate them using N samples as follows:

$$\begin{aligned} \hat{\mu}(x, y) &= \frac{1}{N} \sum_{i=1}^N \tilde{\mathbf{R}}^i(x, y), \\ \hat{\sigma}^2(x, y) &= \frac{1}{N} \sum_{i=1}^N \left(\tilde{\mathbf{R}}^i(x, y) - \hat{\mu}(x, y) \right)^2. \end{aligned} \quad (5)$$

In our implementation, we utilize synthetic data as the source of ground-truth depth maps, adapting the latent diffusion model as the underlying diffusion process. Details can be found in Sec. 4.1.

Variance vs. Reliability. In the Bayesian perspective, running the denoising process corresponds to drawing samples from the learned posterior distribution:

$$p(\mathbf{D}_{\text{true}} \mid \mathbf{I}, \mathbf{D}_{\text{cond}}, \mathbf{M}), \quad (6)$$

where $\mathbf{D}_{\text{cond}} = \mathbf{D}_{\text{raw}}$ during inference. At the pixel level, the posterior can be expressed as:

$$p(\mathbf{D}_{\text{true},(i,j)} \mid \mathbf{I}, \mathbf{D}_{\text{cond}}, \mathbf{M}). \quad (7)$$

Using Bayes’ theorem, this posterior can be approximated as:

$$p(\mathbf{D}_{\text{true},(i,j)} \mid \mathbf{I}, \mathbf{D}_{\text{cond}}, \mathbf{M}) \propto p(\mathbf{D}_{\text{cond},(i,j)} \mid \mathbf{D}_{\text{true},(i,j)})p(\mathbf{D}_{\text{true},(i,j)} \mid \mathbf{I}, \mathbf{M}). \quad (8)$$

Here, the likelihood term $p(\mathbf{D}_{\text{cond},(i,j)} \mid \mathbf{D}_{\text{true},(i,j)})$ quantifies how well the input depth aligns with the ground-truth depth, whereas the prior term $p(\mathbf{D}_{\text{true},(i,j)} \mid \mathbf{I}, \mathbf{M})$ encodes the model’s learned knowledge of plausible depth values based on the RGB image and the missing mask. For detailed derivations, we refer readers to the appendix.

In summary, Eq. 8 suggests that (i) when the captured depth \mathbf{D}_{raw} is reliable (i.e., it aligns well with the training data), the likelihood term becomes sharply peaked, yielding a narrow posterior and low posterior variance. (ii) Conversely, if the captured depth \mathbf{D}_{raw} is unreliable, the likelihood becomes weak, and the prior term exerts more influence on the posterior. However, the prior alone may not provide sufficient information to fully resolve the uncertainty, resulting in a broader posterior and higher variance. Thus by identifying high-variance regions, we can selectively refine the most uncertain areas using a deterministic model, ensuring a more reliable depth reconstruction.

Remarks. In our formulation, we treat missing regions separately from other artifacts, as detecting missing areas is straightforward and computationally inexpensive. However, based on Eq. 8, both artifacts and missing areas share a common property: they exhibit weak likelihood terms and rely more heavily on the learned prior in the model. This observation implies that missing areas and artifacts behave similarly in terms of μ and σ^2 . As a result, by filtering out unreliable depth measurements based on σ^2 during subsequent refinement, we primarily focus on the missing areas in the subsequent deterministic step. This simplification reduces the complexity of the training process, making it easier and more efficient to train the refinement network.

Furthermore, recent studies on depth have shown that excluding artifacts from real-world data brings synthetic datasets closer to their distribution [31, 40]. This supports the idea that the likelihood term in Eq. 8 aligns well with reliable regions, enabling the refinement network to be trained solely on synthetic data while still performing effectively in real-world scenarios.

3.2. Deterministic refinement

Recall that in Sec 3.1, the depth map used during training is scale-shift normalized, so the actual metric range of the depth map is missing. In addition, because the diffusion process is global and stochastic, it is less effective for pixel-level corrections. Accordingly, we employ a deterministic refinement network to restore the metric range and further refine depth at the pixel-level.

Our refinement network is inspired by the sparsity-adaptive depth refinement (SDR) framework [30], which refines monocular depth estimates using sparse depth measurements. SDR utilizes the masked spatial propagation, where refinement starts from reliable depth values and progressively updates nearby pixels along with an evolving propagation mask. This ensures that reliable depth information is effectively propagated while refining unreliable depth estimates. We adopt this framework to complement our diffusion model by restoring absolute depth scales and improving pixel-level accuracy while preserving structural consistency.

We first filter out unreliable pixels using $\hat{\sigma}^2$ derived in Sec 3.1. A certainty mask $\mathbf{M}_{\hat{\sigma}^2} \in \mathbb{R}^{H \times W}$ is defined as:

$$\mathbf{M}_{\hat{\sigma}^2}(x, y) = \begin{cases} 0, & \text{if } \hat{\sigma}^2(x, y) > \epsilon, \\ 1, & \text{otherwise.} \end{cases} \quad (9)$$

Using this mask, we define a depth map with reliable values \mathbf{D}_{rel} and a scaled relative depth map $\mathbf{D}_{\hat{\mu}}$ as follows:

$$\mathbf{D}_{\text{rel}} = \mathbf{D}_{\text{cond}} \otimes \mathbf{M} \otimes \mathbf{M}_{\hat{\sigma}^2}, \quad \mathbf{D}_{\hat{\mu}} = a \cdot \hat{\mu} + b \quad (10)$$

where \otimes denotes the Hadamard (element-wise) product. To remove small artifacts from hard thresholding, we apply morphological opening to $\mathbf{M}_{\hat{\sigma}^2}$ before computing \mathbf{D}_{rel} . The scale and shift parameters a and b are obtained by solving the least-squares problem:

$$\{a, b\} = \arg \min_{a, b} \|\mathbf{D}_{\text{rel}} - (a \cdot \hat{\mu} + b)\|^2. \quad (11)$$

Next, we extract a guidance feature \mathbf{G} using a feature extraction module Φ_{guide} , which encodes both global context and local uncertainty cues. The guidance feature is formulated as:

$$\mathbf{G} = \Phi_{\text{guide}}(\mathbf{I}, \mathbf{D}_{\text{rel}}, \mathbf{D}_{\hat{\mu}}, \hat{\sigma}^2). \quad (12)$$

In Eq. 12, including \mathbf{D}_{rel} , $\mathbf{D}_{\hat{\mu}}$, and $\hat{\sigma}^2$ provides complementary information that enhances the refinement process. \mathbf{D}_{rel} retains only depth values deemed trustworthy based on the certainty mask, serving as a reliable reference. However, filtering removes noisy depth values at the cost of increased sparsity, which may disrupt global consistency.

On the other hand, $\mathbf{D}_{\hat{\mu}}$ retains the global scene structure from the diffusion network while restoring absolute depth scales via least-squares fitting, ensuring geometric coherence. Additionally, $\hat{\sigma}^2$ encodes pixel-wise uncertainty,

allowing the network to adaptively update weights during masked spatial propagation. By combining these three components, the guidance feature \mathbf{G} provides a strong structural prior with metric scale information while preserving both global consistency and local adaptability, thus ensuring effective depth refinement.

With \mathbf{G} , we iteratively refine the depth map using the masked spatial propagation module Φ_{MSPN} , as proposed in [30]. The refinement process starts with the initial depth map \mathcal{D}^0 and mask \mathcal{M}^0 defined as:

$$\mathcal{D}^0 = \mathbf{D}_{\text{rel}}, \quad \mathcal{M}^0 = \mathbf{M} \otimes \mathbf{M}_{\hat{\sigma}^2}. \quad (13)$$

At each iteration k , the depth map \mathcal{D}^k and mask \mathcal{M}^k are updated as follows:

$$(\mathcal{D}^{k+1}, \mathcal{M}^{k+1}) = \Phi_{\text{MSPN}}(\mathcal{D}^k, \mathcal{M}^k, \mathbf{G}), \quad k = 0, \dots, K-1, \quad (14)$$

where K is the total number of iterations. The final refined depth map is obtained as $\mathbf{D}_{\text{refined}} = \mathcal{D}^K$.

This refinement pipeline applies localized corrections to uncertain regions identified by $\hat{\sigma}^2$, yielding $\mathbf{D}_{\text{refined}}$ with improved structural coherence and robustness to sensor noise. By leveraging the complementary strengths of stochastic diffusion for global consistency and deterministic refinement for local accuracy, our two-stage framework effectively balances global plausibility with pixel-level precision, thereby mitigating the limitations inherent to each individual method.

To train our deterministic refinement network, we also use the outputs of our diffusion model also on synthetic data. For each sample, we randomly generate a mask \mathbf{M} and compute \mathbf{D}_{cond} from \mathbf{D}_{true} . Then, we perform inference through the diffusion model to obtain $\hat{\mu}$ and $\hat{\sigma}^2$. We treat $(\mathbf{D}_{\text{cond}}, \hat{\mu}, \hat{\sigma}^2)$ as inputs, and optimize the refinement network by minimizing the error against the known ground-truth depth \mathbf{D}_{true} using L1 and L2 loss, following [30].

This training strategy enables the refinement network to leverage the posterior estimates of the stochastic diffusion model while still preserving metric accuracy through supervised learning on synthetic ground truth.

Remarks. To prevent the network from overfitting to the specific metric range in the training dataset, we want the network to infer the metric range directly from the raw depth map \mathbf{D}_{raw} . To achieve this, we apply a random scale and shift to the depth data during training of the deterministic network. This strategy enhances the generalizability of our method to in real-world data, where the metric range may vary significantly. Furthermore, it facilitates the integration of multiple datasets with differing metric ranges, enabling the scalability of our model to larger and more diverse training datasets.

RMSE	$\frac{1}{ \mathbf{D} } \left(\sum_i (\hat{d}_i - d_i)^2 \right)^{0.5}$
δ_k	% of d_i that satisfies $\max \left\{ \frac{\hat{d}_i}{d_i}, \frac{d_i}{\hat{d}_i} \right\} < k$
Kendall's τ	$\frac{\alpha(\hat{D}, D) - \beta(\hat{D}, D)}{\binom{ \mathbf{D} }{2}}$

Table 1. Evaluation metrics for estimated depth maps. Here, $|\mathbf{D}|$ denotes the number of valid pixels in a depth map \mathbf{D} , d_i is the i th valid depth in \mathbf{D} , and \hat{d}_i is an estimate of d_i . $\alpha(\cdot)$ and $\beta(\cdot)$ count the number of concordant and discordant depth pairs, respectively.

Method	Train data	DIODE-Indoor			NYUv2		
		RMSE \downarrow	$\delta_{1.25}\uparrow$	$\tau\uparrow$	RMSE \downarrow	$\delta_{1.25}\uparrow$	$\tau\uparrow$
DA V1 [64]	Raw data	0.837	0.719	0.819	0.282	0.959	0.838
	Diff. only	0.818	0.725	0.803	0.246	0.960	0.864
	Proposed	0.816	0.727	0.820	0.223	0.974	0.873
DA V2 [65]	Raw data	0.828	0.724	0.845	0.263	0.965	0.846
	Diff. only	0.821	0.719	0.821	0.249	0.955	0.867
	Proposed	0.817	0.725	0.851	0.217	0.972	0.877

Table 2. Fine-tuning performance of relative depth estimators using DIODE-Indoor. τ denotes Kendall's τ .

4. Experiments

4.1. Implementation details

Training dataset: We train our framework on the Hypersim dataset [50], a synthetic indoor dataset with dense per-pixel ground-truth depth \mathbf{D}_{true} . This ground truth is essential for our formulation in Eq. 2, where we construct \mathbf{D}_{true} by applying structured masking to \mathbf{D}_{true} during training.

Although a synthetic outdoor dataset, Virtual Kitti 2 [7], can be used for training, it is designed for autonomous driving scenarios with lower variability. We therefore utilize Hypersim for training and evaluate the framework on indoor datasets.

Evaluation dataset: To evaluate the performance of the proposed framework, we adopt three commonly used real-world indoor datasets, DIODE-Indoor [59], NYUv2 [55], and ScanNet [13]. DIODE-Indoor provides dense but noisy data. Meanwhile, NYUv2 and ScanNet provide relatively clean depth maps, but include missing regions. For all experiments, we set $\epsilon = 0.01$.

Diffusion network: We fine-tune Stable Diffusion v2 [51], a latent diffusion model trained on LAION-5B [53]. The VAE remains frozen and encodes inputs, while the denoising U-Net is modified to accept a 16-channel input. The final depth reconstruction is obtained by averaging the decoded VAE output across channels.

Refinement network: For refinement, we employ MaxViT [58] as the feature extractor Φ_{guide} and utilize MSPN [30] for masked spatial propagation. Refinement is performed iteratively over six steps, with two MSPN layers in series (window sizes 13 and 3).

Training details: More details are provided in appendix.

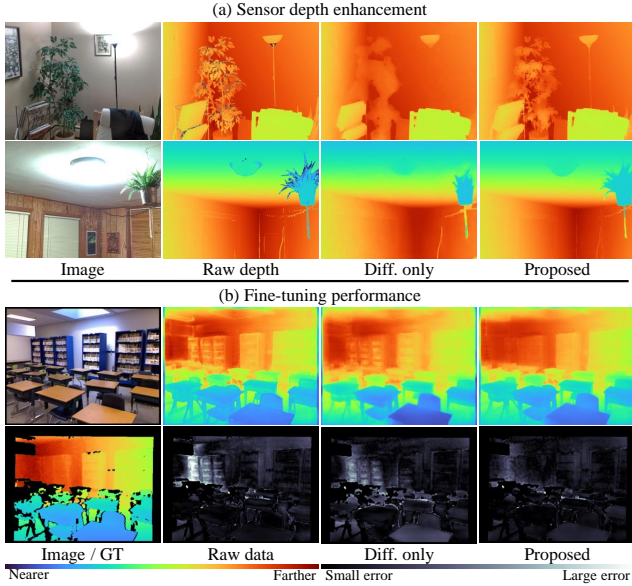


Figure 3. (a) Sensor depth enhancement result on DIODE-Indoor. (b) Qualitative comparison of fine-tuning results on NYUv2. For each depth map in (b), the corresponding error map is provided below, in which brighter pixels represent large errors.

4.2. Evaluation metrics

As described in Tab. 1, we adopt two metrics to measure the quality of metric depth map. For the sensor depth enhancement experiment in Sec 4.3, we additionally adopt Kendall’s τ [33] to measure the accuracy for relative depth.

4.3. Sensor depth enhancement

We assess our sensor depth enhancement framework using the noisy DIODE-Indoor dataset [59]. Since obtaining ground-truth D_{true} is often infeasible, direct evaluation on individual depth maps is challenging. Hence, we conduct an indirect evaluation by fine-tuning relative depth estimators on the refined depth maps and assessing their performance. For this experiment, we adopt Depth Anything (DA) V1 and V2 [64, 65], neither of which was originally trained on DIODE-Indoor. We fine-tune each network five times and report the average performance.

To compare the effectiveness of our framework, we set three training data configurations. ‘Raw data’ refers to the original sensor depth maps without any enhancement. ‘Diff. only’ first removes unreliable pixels using the uncertainty map from our stochastic estimation stage. The same diffusion model is then re-applied to inpaint those missing regions, followed by least squares fitting to recover the global scale as in Eq. 11. ‘Proposed’ represents the full pipeline, incorporating both stochastic estimation and deterministic refinement.

Since the test labels in DIODE-Indoor are noisy as well, we filter out unreliable pixels using $\hat{\sigma}^2$ from the first stage of our pipeline and measure metric depth performance. Ad-

Method	5%		10%		20%	
	RMSE $_{\downarrow}$	$\delta_{1.25\uparrow}$	RMSE $_{\downarrow}$	$\delta_{1.25\uparrow}$	RMSE $_{\downarrow}$	$\delta_{1.25\uparrow}$
CFormer [70]	0.261	0.976	0.370	0.952	0.526	0.897
+ Proposed	0.216	0.972	0.219	0.971	0.225	0.970
MSPN [30]	0.301	0.972	0.437	0.947	0.655	0.888
+ Proposed	0.216	0.972	0.220	0.971	0.227	0.970

Table 3. Noisy depth completion and its refinement performance on NYUv2 using 500 sparse depths. % denotes the noise ratio.

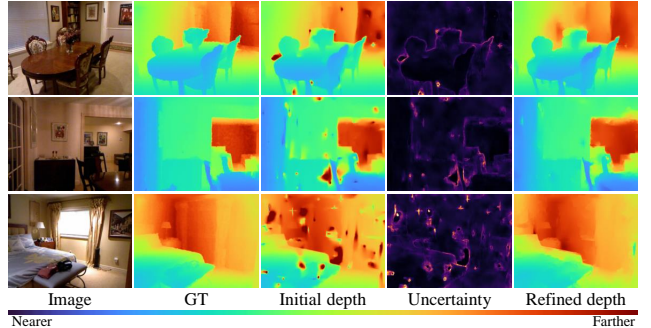


Figure 4. Refinement result on noisy depth completion using MSPN. From the first row, noise ratios are 5%, 10%, and 20%, respectively.

ditionally, we evaluate zero-shot relative depth estimation performance on the NYUv2 test set, a widely used benchmark for depth estimation. This dual evaluation confirms that our framework not only improves data quality in noisy regions but also generalizes well across datasets. The following observations can be made from Tab. 2 and Fig. 3:

- In Tab. 2, we see that ‘Proposed’ consistently outperforms its alternatives not only on DIODE-Indoor but also on NYUv2, demonstrating strong cross-dataset generalization. Specifically, for DA V2, ‘Proposed’ improves RMSE and τ by 21.2% and 4.2%, respectively, compared with ‘Raw data.’
- As illustrated in Fig. 3 (a), ‘Raw data’ contains noisy pixels, particularly around edge regions. ‘Diff. only’ suppresses such noise but often results in blurry refinements. In contrast, ‘Proposed’ effectively reduces structured noise while preserving fine edge details.
- These characteristics are also reflected in the fine-tuned results, as illustrated in Fig. 3 (b). The improved depth quality leads to more accurate predictions in a downstream task.
- Notably, ‘Raw data’ tends to learn incorrect depth values near edge regions, as seen in Fig. 3 (b). While fine-tuning reveals larger disparities in challenging edges, the performance gap in DIODE-Indoor appears smaller since noisy pixels are removed before evaluation. In contrast, for the cleaner NYUv2 dataset, ‘Proposed’ achieves even greater improvements.
- Overall, our framework enhances depth quality by mitigating noise, thus effectively providing higher-quality depth maps for downstream tasks.

Dataset	Method	H2I \in (0.01, 0.1]		H2I \in (0.1, 0.2]		H2I \in (0.2, 0.3]		H2I \in (0.3, 0.4]		H2I \in (0.4, 0.5]		Average	
		RMSE \downarrow	$\delta_{1.25}\uparrow$	RMSE \downarrow	$\delta_{1.25}\uparrow$	RMSE \downarrow	$\delta_{1.25}\uparrow$	RMSE \downarrow	$\delta_{1.25}\uparrow$	RMSE \downarrow	$\delta_{1.25}\uparrow$	RMSE \downarrow	$\delta_{1.25}\uparrow$
NYUv2	Depth Anything V1 [64]	0.460	0.894	0.396	0.869	0.412	0.866	0.417	0.871	0.413	0.861	0.420	0.872
	Depth Anything V2 [65]	0.460	0.887	0.400	0.864	0.418	0.861	0.422	0.863	0.417	0.853	0.423	0.866
	Marigold [31]	0.336	0.931	0.296	0.919	0.315	0.916	0.315	0.921	0.299	0.917	0.312	0.921
	Proposed	0.261	0.954	0.213	0.968	0.216	0.965	0.296	0.941	0.305	0.931	0.259	0.952
ScanNet	Depth Anything V1 [64]	0.220	0.920	0.210	0.916	0.210	0.917	0.208	0.917	0.212	0.916	0.212	0.917
	Depth Anything V2 [65]	0.224	0.919	0.218	0.915	0.217	0.915	0.217	0.916	0.219	0.913	0.219	0.916
	Marigold [31]	0.225	0.905	0.216	0.902	0.219	0.901	0.220	0.910	0.218	0.898	0.220	0.903
	Proposed	0.110	0.974	0.104	0.984	0.115	0.980	0.140	0.970	0.162	0.960	0.126	0.974

Table 4. Depth inpainting performance on NYUv2 and ScanNet according to the hole-to-image (H2I) area ratios.

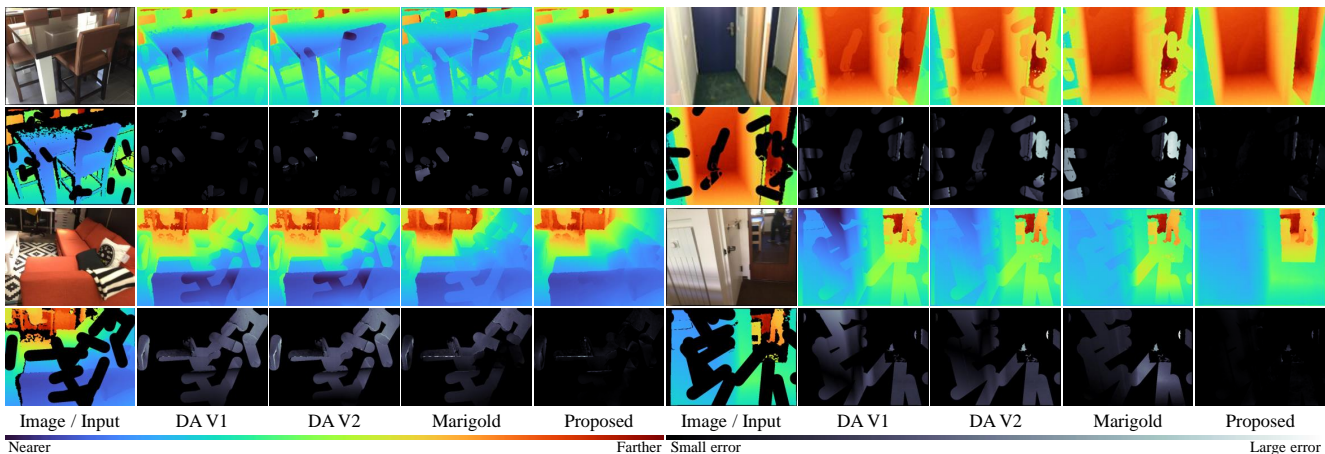


Figure 5. Qualitative comparison of depth inpainting results on ScanNet. For each depth map, the corresponding error map is provided below, in which brighter pixels represent large errors.

4.4. Noisy depth completion

Although directly enhancing real sensor depth is challenging, we can still evaluate the robustness of our framework by injecting sensor-like noise in a controlled setting. To this end, we conduct a refinement experiment on noisy depth completion results, where our approach is applied to remove induced artifacts and improve depth quality.

Conventional depth completion methods generate dense maps from sparse, noise-free measurements. However, real-world sensor depth is often corrupted by noise due to hardware limitations and environmental factors, leading to artifacts that degrade depth accuracy. To assess how well different methods handle such artifacts, we simulate noisy depth completion conditions by introducing noise into the sparse depth inputs. Specifically, we randomly select valid pixels from the ground truth, designate a fraction (5%, 10%, and 20%) as noisy, and add Gaussian noise while ensuring non-negative depth values.

Unlike synthetic depth datasets or artificially degraded clean data, our noisy depth simulation more closely reflects real-world sensor noise, as it introduces a diverse range of artifacts beyond simple pixel-wise corruption. This setting allows us to evaluate not only robustness to synthetic noise but also the ability to refine the structured sensor artifacts that may appear in real-world depth data.

For this experiment, we evaluate our approach alongside a depth completion method, CFormer [70]. Additionally, we test MSPN [30], an SDR framework, which leverages monocular depth estimation as a prior. Tab. 3 and Fig. 4 reveals the following observations:

- In Tab. 3, our framework consistently improves the noisy depth completion across varying noise levels. Although trained solely on synthetic data, it generalizes well to real-world artifacts, making it a promising solution for sensor depth refinement.
- At higher noise ratios, conventional methods degrade significantly, whereas our framework maintains robustness, effectively suppressing noise in challenging conditions. For instance, it improves MSPN’s RMSE performance by 289%.
- In Fig. 4, our approach excels in structured regions, enhancing consistency and preserving geometric details.
- These results also validate our designed train-inference domain gap in Sec. 3.1. This discrepancy enables uncertainty estimation and selective refinement, enhancing the adaptability to real-world sensor artifacts.

4.5. Depth inpainting

Our framework demonstrated strong performance in noisy depth maps in Sec. 4.3 and 4.4. However, handling depth maps with large missing area poses a different challenge. In

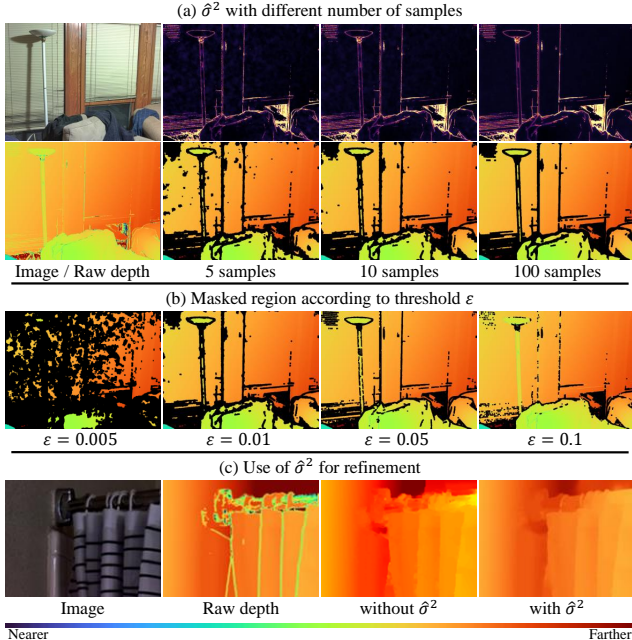


Figure 6. (a) Visualization of $\hat{\sigma}^2$ and the corresponding masked depth map according to N . (b) Masking result according to threshold ϵ . (c) Efficacy of $\hat{\sigma}^2$ for refinement.

such cases, one potential alternative is to leverage a monocular relative depth estimator, where known depth values can be used to recover the global scale of missing regions.

To assess this, we evaluate our diffusion network for inpainting against state-of-the-art monocular relative depth estimators [31, 64, 65]. In this test, we mask out portions of the ground-truth depth maps according to predefined hole-to-image (H2I) area ratios, following existing image inpainting approaches [35, 39, 60]. Specifically, we randomly remove depth values within predefined H2I ranges, ensuring a controlled evaluation of inpainting performance. Next, we apply each monocular depth estimators to reconstruct the occluded areas, then we recover the metric scale using Eq. 11. The evaluation focused on the masked regions. From Tab. 4 and Fig. 5, we observe:

- Monocular methods show stable performance across different H2I ratios, as they primarily rely on contextual cues from RGB inputs. However, they struggle to reconstruct depth accurately in small missing regions, as they do not explicitly incorporate available depth measurements.
- In contrast, ‘Proposed’ consistently outperforms monocular methods across most H2I ratios, particularly when sufficient depth priors are available. For example, at $H2I \in (0.01, 0.1]$, ‘Proposed’ achieves over 50% lower RMSE compared with existing approaches, demonstrating its ability to effectively integrate partial depth priors and maintain global consistency.
- The qualitative results in Fig. 5 further highlight this advantage. While monocular estimators often fail to recon-

struct fine structures and introduce artifacts in large missing regions, ‘Proposed’ preserves geometric details and depth consistency.

- These properties also enable scale-independent learning in the refinement stage of our framework. As discussed in Sec. 3.2, our deterministic refinement network operates on scale-normalized depth inputs, ensuring that the model refines depth maps without being restricted to a fixed metric range. This allows our framework to generalize across datasets with varied depth distributions while still maintaining metric accuracy.

4.6. Analysis

Number of samples: Our uncertainty estimation relies on $\hat{\sigma}^2$ obtained from multiple diffusion samples. Fig. 6 (a) is an example of the uncertainty map and its corresponding masked depth map as N changes. We see that beyond 10 samples, additional samples provide minimal gains but increases inference time. Hence, we set $N = 10$.

Threshold ϵ : Fig. 6 (b) illustrates the masked region of a depth map given different threshold values ϵ . Notably, even with a fixed $\epsilon = 0.01$ most noise artifacts are effectively removed while retaining valid depth structures. This indicates that a simple thresholding approach with a fixed ϵ is sufficient for robust depth refinement.

$\hat{\sigma}^2$ for refinement: To evaluate the benefit of incorporating $\hat{\sigma}^2$ into the refinement stage, we compare the refinement results with and without using $\hat{\sigma}^2$ in Fig. 6 (c). Incorporating $\hat{\sigma}^2$ leads to more stable and accurate refinement results.

5. Conclusions and Limitations

We introduced Perfecting Depth, a novel two-stage framework for sensor depth enhancement. Unlike previous methods, our approach eliminates the need for hand-crafted priors on unreliable pixels. Instead, we employ stochastic estimation to detect artifacts and infer structural priors via a carefully designed training-inference gap, followed by deterministic refinement to ensure consistency and precision.

Despite being trained exclusively on synthetic data, our framework generalizes well to real sensor depth, demonstrating robust performance across diverse scenarios. Moreover, its training strategy prevents memorization of the metric range from training data, enabling scalability with larger and more diverse datasets. By integrating stochastic uncertainty modeling with deterministic refinement, Perfecting Depth establishes a new baseline for sensor depth enhancement.

However, our normalization process requires an additional mask for infinite-depth regions (e.g., sky); otherwise, extreme values risk compressing smaller valid depths into a narrow range, degrading performance. Incorporating insights from adaptive ordinal regression [5] could further refine accuracy and enhance texture details.

References

- [1] Miguel Angel Bautista, Pengsheng Guo, Samira Abnar, Walter Talbott, Alexander Toshev, Zhuoyuan Chen, Laurent Dinh, Shuangfei Zhai, Hanlin Goh, Daniel Ulbricht, et al. GAUDI: A neural architect for immersive 3d scene generation. In *NeurIPS*, 2022. 2
- [2] Lucas Berry and David Meger. Escaping the sample trap: Fast and accurate epistemic uncertainty estimation with pairwise-distance estimators. 2023. 3
- [3] Lucas Berry and David Meger. Normalizing flow ensembles for rich aleatoric and epistemic uncertainty modeling. In *Proceedings of the AAAI Conference on Artificial Intelligence*, pages 6806–6814, 2023.
- [4] Lucas Berry, Axel Brando, and David Meger. Shedding light on large generative networks: Estimating epistemic uncertainty in diffusion models. In *The 40th Conference on Uncertainty in Artificial Intelligence*, 2024. 3
- [5] Shariq Farooq Bhat, Ibraheem Alhashim, and Peter Wonka. AdaBins: Depth estimation using adaptive bins. In *CVPR*, 2021. 1, 8
- [6] Andreas Blattmann, Robin Rombach, Huan Ling, Tim Dockhorn, Seung Wook Kim, Sanja Fidler, and Karsten Kreis. Align your latents: High-resolution video synthesis with latent diffusion models. In *CVPR*, 2023. 2
- [7] Johann Cabon, Naila Murray, and Martin Humenberger. Virtual kitti 2. *arXiv preprint arXiv:2001.10773*, 2020. 5
- [8] Xinjing Cheng, Peng Wang, and Ruigang Yang. Depth estimation via affinity learned with convolutional spatial propagation network. In *ECCV*, 2018. 2
- [9] Xinjing Cheng, Peng Wang, and Ruigang Yang. Learning depth with convolutional spatial propagation network. *IEEE transactions on pattern analysis and machine intelligence*, 42(10):2361–2379, 2019. 2
- [10] Hyunsun Choi, Eric Jang, and Alexander A Alemi. Waic, but why? generative ensembles for robust anomaly detection. *arXiv preprint arXiv:1810.01392*, 2018. 3
- [11] Kurtland Chua, Roberto Calandra, Rowan McAllister, and Sergey Levine. Deep reinforcement learning in a handful of trials using probabilistic dynamics models. *Advances in neural information processing systems*, 31, 2018. 3
- [12] Andrea Conti, Matteo Poggi, and Stefano Mattoccia. Sparsity agnostic depth completion. In *WACV*, 2023. 2
- [13] Angela Dai, Angel X. Chang, Manolis Savva, Maciej Halber, Thomas Funkhouser, and Matthias Nießner. ScanNet: Richly-annotated 3D reconstructions of indoor scenes. In *CVPR*, 2017. 5, 12, 14
- [14] Stefan Depeweg, Jose-Miguel Hernandez-Lobato, Finale Doshi-Velez, and Steffen Udluft. Decomposition of uncertainty in bayesian deep learning for efficient and risk-sensitive learning. In *International conference on machine learning*, pages 1184–1193. PMLR, 2018. 3
- [15] Jacob Devlin, Ming-Wei Chang, Kenton Lee, and Kristina Toutanova. BERT: Pre-training of deep bidirectional transformers for language understanding. In *NAACL*, 2018. 2
- [16] Prafulla Dhariwal and Alexander Nichol. Diffusion models beat gans on image synthesis. In *NeurIPS*, 2021. 2
- [17] Alexey Dosovitskiy, Lucas Beyer, Alexander Kolesnikov, Dirk Weissenborn, Xiaohua Zhai, Thomas Unterthiner, Mostafa Dehghani, Matthias Minderer, Georg Heigold, Sylvain Gelly, Jakob Uszkoreit, and Neil Houlsby. An image is worth 16x16 words: Transformers for image recognition at scale. In *ICLR*, 2021. 2
- [18] Ruofei Du, Eric Turner, Maksym Dzitsiuk, Luca Prasso, Ivo Duarte, Jason Dourgarian, Joao Afonso, Jose Pascoal, Josh Gladstone, Nuno Cruces, et al. Depthlab: Real-time 3d interaction with depth maps for mobile augmented reality. In *UIST*, 2020. 1
- [19] David Eigen, Christian Puhrsch, and Rob Fergus. Depth map prediction from a single image using a multi-scale deep network. In *NeurIPS*, 2014. 1
- [20] Patrick Esser, Johnathan Chiu, Parmida Atighehchian, Jonathan Granskog, and Anastasis Germanidis. Structure and content-guided video synthesis with diffusion models. In *ICCV*, 2023. 2
- [21] Huan Fu, Mingming Gong, Chaohui Wang, Kayhan Batmanghelich, and Dacheng Tao. Deep ordinal regression network for monocular depth estimation. In *CVPR*, 2018. 1
- [22] Xiao Fu, Wei Yin, Mu Hu, Kaixuan Wang, Yuexin Ma, Ping Tan, Shaojie Shen, Dahua Lin, and Xiaoxiao Long. Geowizard: Unleashing the diffusion priors for 3d geometry estimation from a single image. In *ECCV*, 2024. 1, 2
- [23] Yarin Gal, Riashat Islam, and Zoubin Ghahramani. Deep bayesian active learning with image data. In *International conference on machine learning*, pages 1183–1192. PMLR, 2017. 3
- [24] Andreas Geiger, Philip Lenz, and Raquel Urtasun. Are we ready for autonomous driving? the KITTI vision benchmark suite. In *CVPR*, 2012. 1
- [25] Kaiming He, Xinlei Chen, Saining Xie, Yanghao Li, Piotr Dollár, and Ross Girshick. Masked autoencoders are scalable vision learners. In *CVPR*, 2022. 2
- [26] Lingzhi He, Hongguang Zhu, Feng Li, Huihui Bai, Runmin Cong, Chunjie Zhang, Chunyu Lin, Meiqin Liu, and Yao Zhao. Towards fast and accurate real-world depth super-resolution: Benchmark dataset and baseline. In *CVPR*, 2021. 2
- [27] Jonathan Ho, Ajay Jain, and Pieter Abbeel. Denoising diffusion probabilistic models. In *NeurIPS*, 2020. 2
- [28] Hamid Izadinia, Qi Shan, and Steven M. Seitz. IM2CAD. In *CVPR*, 2017. 1
- [29] Yuanfeng Ji, Zhe Chen, Enze Xie, Lanqing Hong, Xihui Liu, Zhaoqiang Liu, Tong Lu, Zhenguo Li, and Ping Luo. DDP: Diffusion model for dense visual prediction. In *ICCV*, 2023. 2
- [30] Jinyoung Jun, Jae-Han Lee, and Chang-Su Kim. Masked spatial propagation network for sparsity-adaptive depth refinement. In *CVPR*, 2024. 2, 4, 5, 6, 7, 12, 14
- [31] Bingxin Ke, Anton Obukhov, Shengyu Huang, Nando Metzger, Rodrigo Caye Daudt, and Konrad Schindler. Repurposing diffusion-based image generators for monocular depth estimation. In *CVPR*, 2024. 1, 2, 4, 7, 8, 12
- [32] Alex Kendall and Yarin Gal. What uncertainties do we need in bayesian deep learning for computer vision? *Advances in neural information processing systems*, 30, 2017. 3

- [33] Maurice G. Kendall. A new measure of rank correlation. *Biometrika*, 30(1/2):81–93, 1938. [6](#)
- [34] Andreas Kirsch, Joost Van Amersfoort, and Yarin Gal. Batchbald: Efficient and diverse batch acquisition for deep bayesian active learning. *Advances in neural information processing systems*, 32, 2019. [3](#)
- [35] Keunsoo Ko and Chang-Su Kim. Continuously masked transformer for image inpainting. In *ICCV*, 2023. [8](#)
- [36] Balaji Lakshminarayanan, Alexander Pritzel, and Charles Blundell. Simple and scalable predictive uncertainty estimation using deep ensembles. *Advances in neural information processing systems*, 30, 2017. [3](#)
- [37] Jae-Han Lee, Minhyeok Heo, Kyung-Rae Kim, and Chang-Su Kim. Single-image depth estimation based on Fourier domain analysis. In *CVPR*, 2018. [1](#)
- [38] Jin Han Lee, Myung-Kyu Han, Dong Wook Ko, and Il Hong Suh. From big to small: Multi-scale local planar guidance for monocular depth estimation. *arXiv preprint arXiv:1907.10326*, 2019. [1](#)
- [39] Wenbo Li, Zhe Lin, Kun Zhou, Lu Qi, Yi Wang, and Jiaya Jia. Mat: Mask-aware transformer for large hole image inpainting. In *CVPR*, 2022. [8](#)
- [40] Zhiheng Liu, Ka Leong Cheng, Qiuyu Wang, Shuzhe Wang, Hao Ouyang, Bin Tan, Kai Zhu, Yujun Shen, Qifeng Chen, and Ping Luo. Depthlab: From partial to complete. *arXiv preprint arXiv:2412.18153*, 2024. [2, 4](#)
- [41] Fangchang Ma and Sertac Karaman. Sparse-to-dense: Depth prediction from sparse depth samples and a single image. In *ICRA*, 2018. [2](#)
- [42] Nando Metzger, Rodrigo Caye Daudt, and Konrad Schindler. Guided depth super-resolution by deep anisotropic diffusion. In *CVPR*, 2023. [2](#)
- [43] Sicheng Mo, Fangzhou Mu, Kuan Heng Lin, Yanli Liu, Bochen Guan, Yin Li, and Bolei Zhou. Freecontrol: Training-free spatial control of any text-to-image diffusion model with any condition. In *CVPR*, 2024. [2](#)
- [44] Danish Nazir, Alain Pagani, Marcus Liwicki, Didier Stricker, and Muhammad Zeshan Afzal. Semattnet: Toward attention-based semantic aware guided depth completion. *IEEE Access*, 10:120781–120791, 2022. [2](#)
- [45] Jinsun Park, Kyungdon Joo, Zhe Hu, Chi-Kuei Liu, and In So Kweon. Non-local spatial propagation network for depth completion. In *ECCV*, 2020. [2](#)
- [46] Jin-Hwi Park, Chanhwi Jeong, Junoh Lee, and Hae-Gon Jeon. Depth prompting for sensor-agnostic depth estimation. In *CVPR*, 2024. [2](#)
- [47] Suraj Patni, Aradhye Agarwal, and Chetan Arora. Ecodepth: Effective conditioning of diffusion models for monocular depth estimation. In *CVPR*, 2024. [2](#)
- [48] Janis Postels, Hermann Blum, Yannick Strümler, Cesar Cadena, Roland Siegwart, Luc Van Gool, and Federico Tombari. The hidden uncertainty in a neural networks activations. *arXiv preprint arXiv:2012.03082*, 2020. [3](#)
- [49] René Ranftl, Katrin Lasinger, David Hafner, Konrad Schindler, and Vladlen Koltun. Towards robust monocular depth estimation: Mixing datasets for zero-shot cross-dataset transfer. *IEEE Trans. Pattern Anal. Mach. Intell.*, 44(3):1623–1637, 2020. [1](#)
- [50] Mike Roberts, Jason Ramapuram, Anurag Ranjan, Atulit Kumar, Miguel Angel Bautista, Nathan Paczan, Russ Webb, and Joshua M Susskind. Hypersim: A photorealistic synthetic dataset for holistic indoor scene understanding. In *ICCV*, 2021. [5, 12](#)
- [51] Robin Rombach, Andreas Blattmann, Dominik Lorenz, Patrick Esser, and Björn Ommer. High-resolution image synthesis with latent diffusion models. In *CVPR*, 2022. [2, 5](#)
- [52] Saurabh Saxena, Charles Herrmann, Junhwa Hur, Abhishek Kar, Mohammad Norouzi, Deqing Sun, and David J Fleet. The surprising effectiveness of diffusion models for optical flow and monocular depth estimation. In *NeurIPS*, 2024. [2](#)
- [53] Christoph Schuhmann, Romain Beaumont, Richard Vencu, Cade Gordon, Ross Wightman, Mehdi Cherti, Theo Coombes, Aarush Katta, Clayton Mullis, Mitchell Wortsman, et al. Laion-5B: An open large-scale dataset for training next generation image-text models. In *NeurIPS*, 2022. [5](#)
- [54] Dule Shu and Amir Barati Farimani. Zero-shot uncertainty quantification using diffusion probabilistic models. *arXiv preprint arXiv:2408.04718*, 2024. [3](#)
- [55] Nathan Silberman, Derek Hoiem, Pushmeet Kohli, and Rob Fergus. Indoor segmentation and support inference from RGBD images. In *ECCV*, 2012. [1, 5, 12, 14](#)
- [56] Jiaming Song, Chenlin Meng, and Stefano Ermon. Denoising diffusion implicit models. In *ICLR*, 2021. [2](#)
- [57] Fabio Tosi, Pierluigi Zama Ramirez, and Matteo Poggi. Diffusion models for monocular depth estimation: Overcoming challenging conditions. In *ECCV*, 2024. [2](#)
- [58] Zhengzhong Tu, Hossein Talebi, Han Zhang, Feng Yang, Peyman Milanfar, Alan Bovik, and Yinxiao Li. Maxvit: Multi-axis vision transformer. In *ECCV*, 2022. [5, 12](#)
- [59] Igor Vasiljevic, Nick Kolkin, Shanyi Zhang, Ruotian Luo, Haochen Wang, Falcon Z. Dai, Andrea F. Daniele, Mohammadreza Mostajabi, Steven Basart, Matthew R. Walter, and Gregory Shakhnarovich. DIODE: A dense indoor and outdoor depth dataset. *arXiv preprint arXiv:1908.00463*, 2019. [5, 6, 12, 13](#)
- [60] Ziyu Wan, Jingbo Zhang, Dongdong Chen, and Jing Liao. High-fidelity pluralistic image completion with transformers. In *ICCV*, 2021. [8](#)
- [61] Yufei Wang, Bo Li, Ge Zhang, Qi Liu, Tao Gao, and Yuchao Dai. Lrru: Long-short range recurrent updating networks for depth completion. In *ICCV*, 2023. [2](#)
- [62] Junyuan Xie, Ross Girshick, and Ali Farhadi. Deep3D: Fully automatic 2D-to-3D video conversion with deep convolutional neural networks. In *ECCV*, 2016. [1](#)
- [63] Zhenda Xie, Zheng Zhang, Yue Cao, Yutong Lin, Jianmin Bao, Zhuliang Yao, Qi Dai, and Han Hu. SimMIM: A simple framework for masked image modeling. In *CVPR*, 2022. [2](#)
- [64] Lihe Yang, Bingyi Kang, Zilong Huang, Xiaogang Xu, Jiashi Feng, and Hengshuang Zhao. Depth Anything: Unleashing the power of large-scale unlabeled data. In *CVPR*, 2024. [1, 5, 6, 7, 8](#)
- [65] Lihe Yang, Bingyi Kang, Zilong Huang, Zhen Zhao, Xiaogang Xu, Jiashi Feng, and Hengshuang Zhao. Depth anything v2. *arXiv:2406.09414*, 2024. [5, 6, 7, 8](#)

- [66] Zhu Yu, Zehua Sheng, Zili Zhou, Lun Luo, Si-Yuan Cao, Hong Gu, Huaqi Zhang, and Hui-Liang Shen. Aggregating feature point cloud for depth completion. In *ICCV*, 2023. 2
- [67] Biao Zhang, Jiapeng Tang, Matthias Niessner, and Peter Wonka. 3dshape2vecset: A 3d shape representation for neural fields and generative diffusion models. *ACM Trans. Graph.*, 42(4):1–16, 2023. 2
- [68] Jingyang Zhang, Shiwei Li, Yuanxun Lu, Tian Fang, David McKinnon, Yanghai Tsin, Long Quan, and Yao Yao. Jointnet: Extending text-to-image diffusion for dense distribution modeling. In *ICLR*, 2023. 2
- [69] Lvmin Zhang, Anyi Rao, and Maneesh Agrawala. Adding conditional control to text-to-image diffusion models. In *ICCV*, 2023. 2
- [70] Youmin Zhang, Xianda Guo, Matteo Poggi, Zheng Zhu, Guan Huang, and Stefano Mattoccia. Completionformer: Depth completion with convolutions and vision transformers. In *CVPR*, 2023. 2, 6, 7, 14
- [71] Wenliang Zhao, Yongming Rao, Zuyan Liu, Benlin Liu, Jie Zhou, and Jiwen Lu. Unleashing text-to-image diffusion models for visual perception. In *ICCV*, 2023. 2
- [72] Zixiang Zhao, Jianshe Zhang, Shuang Xu, Zudi Lin, and Hanspeter Pfister. Discrete cosine transform network for guided depth map super-resolution. In *CVPR*, 2022. 2
- [73] Zixiang Zhao, Jianshe Zhang, Xiang Gu, Chengli Tan, Shuang Xu, Yulun Zhang, Radu Timofte, and Luc Van Gool. Spherical space feature decomposition for guided depth map super-resolution. In *CVPR*, 2023. 2

A. Posterior approximation

In this section, we will discuss about why the variation could serve as a reliable indicator for \mathbf{D}_{raw} . As shown in the main paper, the posterior at the pixel-level could be written as:

$$p(\mathbf{D}_{\text{true},(i,j)} \mid \mathbf{I}, \mathbf{D}_{\text{cond}}, \mathbf{M}),$$

which can be further expanded using Bayes' rule:

$$p(\mathbf{D}_{\text{true},(i,j)} \mid \mathbf{I}, \mathbf{D}_{\text{cond}}, \mathbf{M}) = \frac{p(\mathbf{D}_{\text{cond},(i,j)} \mid \mathbf{D}_{\text{true},(i,j)}) p(\mathbf{D}_{\text{true},(i,j)} \mid \mathbf{I}, \mathbf{M})}{p(\mathbf{D}_{\text{cond},(i,j)} \mid \mathbf{I}, \mathbf{M})}. \quad (15)$$

Here we make two approximations based on the assumption that (1) the depth \mathbf{D}_{cond} relies more on the ground-truth depth \mathbf{D}_{true} at the same pixel (remember that in the training stage the synthetic data is built from the \mathbf{D}_{true}) and (2) the RGB input \mathbf{I} and the missing mask \mathbf{M} are assumed to be independent of the ground-truth depth \mathbf{D}_{true} where they are fixed inputs and do not change based on the depth. To be more specific, the RGB image \mathbf{I} is a fixed input that reflects the appearance of the scene, and its generation does not explicitly depend on the depth values during inference. The mask \mathbf{M} simply indicates missing or invalid regions in the observed depth \mathbf{D} , and is determined by the sensor output (not the actual ground-truth depth). Thus we get:

$$p(\mathbf{D}_{\text{cond}}, \mathbf{I}, \mathbf{M} \mid \mathbf{D}_{\text{true},(i,j)}) \approx p(\mathbf{D}_{\text{cond}} \mid \mathbf{D}_{\text{true},(i,j)}) \cdot p(\mathbf{I}, \mathbf{M}) \quad (16)$$

Substituting the factorized likelihood back into the Bayes' Theorem, we have:

$$\begin{aligned} p(\mathbf{D}_{\text{true},(i,j)} \mid \mathbf{I}, \mathbf{D}_{\text{cond}}, \mathbf{M}) &\approx \frac{p(\mathbf{D}_{\text{cond},(i,j)} \mid \mathbf{D}_{\text{true},(i,j)}) p(\mathbf{I}, \mathbf{M}) p(\mathbf{D}_{\text{true},(i,j)})}{p(\mathbf{D}_{\text{cond}}, \mathbf{I}, \mathbf{M})} \\ &\Rightarrow p(\mathbf{D}_{\text{true},(i,j)} \mid \mathbf{I}, \mathbf{D}_{\text{cond}}, \mathbf{M}) \propto p(\mathbf{D}_{\text{cond},(i,j)} \mid \mathbf{D}_{\text{true},(i,j)}) p(\mathbf{D}_{\text{true},(i,j)}). \end{aligned} \quad (17)$$

At this stage, we recognize that $p(\mathbf{D}_{\text{true},(i,j)})$, the prior on the ground-truth depth, can itself depend on \mathbf{I} and \mathbf{M} . In other words, while $p(\mathbf{D}_{\text{true},(i,j)})$ is the prior distribution for $\mathbf{D}_{\text{true},(i,j)}$, the RGB image \mathbf{I} and the mask \mathbf{M} provide additional context that informs this prior. Therefore, we refine the prior term as:

$$p(\mathbf{D}_{\text{true},(i,j)}) = p(\mathbf{D}_{\text{true},(i,j)} \mid \mathbf{I}, \mathbf{M}).$$

So we have:

$$p(\mathbf{D}_{\text{true},(i,j)} \mid \mathbf{I}, \mathbf{D}_{\text{cond}}, \mathbf{M}) \propto p(\mathbf{D}_{\text{cond},(i,j)} \mid \mathbf{D}_{\text{true},(i,j)}) p(\mathbf{D}_{\text{true},(i,j)} \mid \mathbf{I}, \mathbf{M}), \quad (18)$$

which is exactly Eq. 8 in the main paper. As discussed in the main paper, the likelihood term $p(\mathbf{D}_{\text{cond},(i,j)} \mid \mathbf{D}_{\text{true},(i,j)})$ measures how well the input depth aligns with the ground truth depth, while the prior term $p(\mathbf{D}_{\text{true},(i,j)} \mid \mathbf{I}, \mathbf{M})$ captures the model's learned knowledge of plausible depth values based on the RGB image and the missing mask. In real-world scenarios, when the captured depth \mathbf{D}_{raw} is reliable and closely matches the training data, the likelihood term becomes sharply peaked, resulting in a narrow posterior and low posterior variance. Conversely, if the captured depth is unreliable, the likelihood is weak, giving the prior term greater influence over the posterior. However, if the prior lacks sufficient information to resolve the uncertainty, the posterior becomes broader, leading to higher variance.

B. Training Details

Training Dataset: We sample 54K RGB-D images from the Hypersim dataset [50] to train both the diffusion and refinement networks.

Evaluation Dataset: For DIODE-Indoor [59], we use the official 325-image validation split. For NYUv2 [55], we adopt the official 654-image test set. For ScanNet [13], we evaluate on the 800 validation images as in Marigold [31].

Diffusion Network: We fine-tune the Stable Diffusion U-Net on 4 A100 GPUs (batch size = 48) for 30K iterations, using MSE loss and a learning rate of 3×10^{-5} . During training, random cropping and horizontal flipping are applied to handle variability in field of view and orientation.

Refinement Network: We adopt MaxViT-L [58] as the encoder for the guidance module. Since we have four inputs (\mathbf{I} , \mathbf{D}_{rel} , $\mathbf{D}_{\hat{\mu}}$, and $\hat{\sigma}^2$), each input passes through a shallow convolutional block, and the resulting feature maps are concatenated. We also modify the first convolutional layer to match the new channel dimension. For the decoder, we follow the same architecture used in the original SDR framework [30].

C. Sensor depth enhancement

Fig. 7 illustrates the sensor depth enhancement result of the proposed framework on DIODE-Indoor [59].

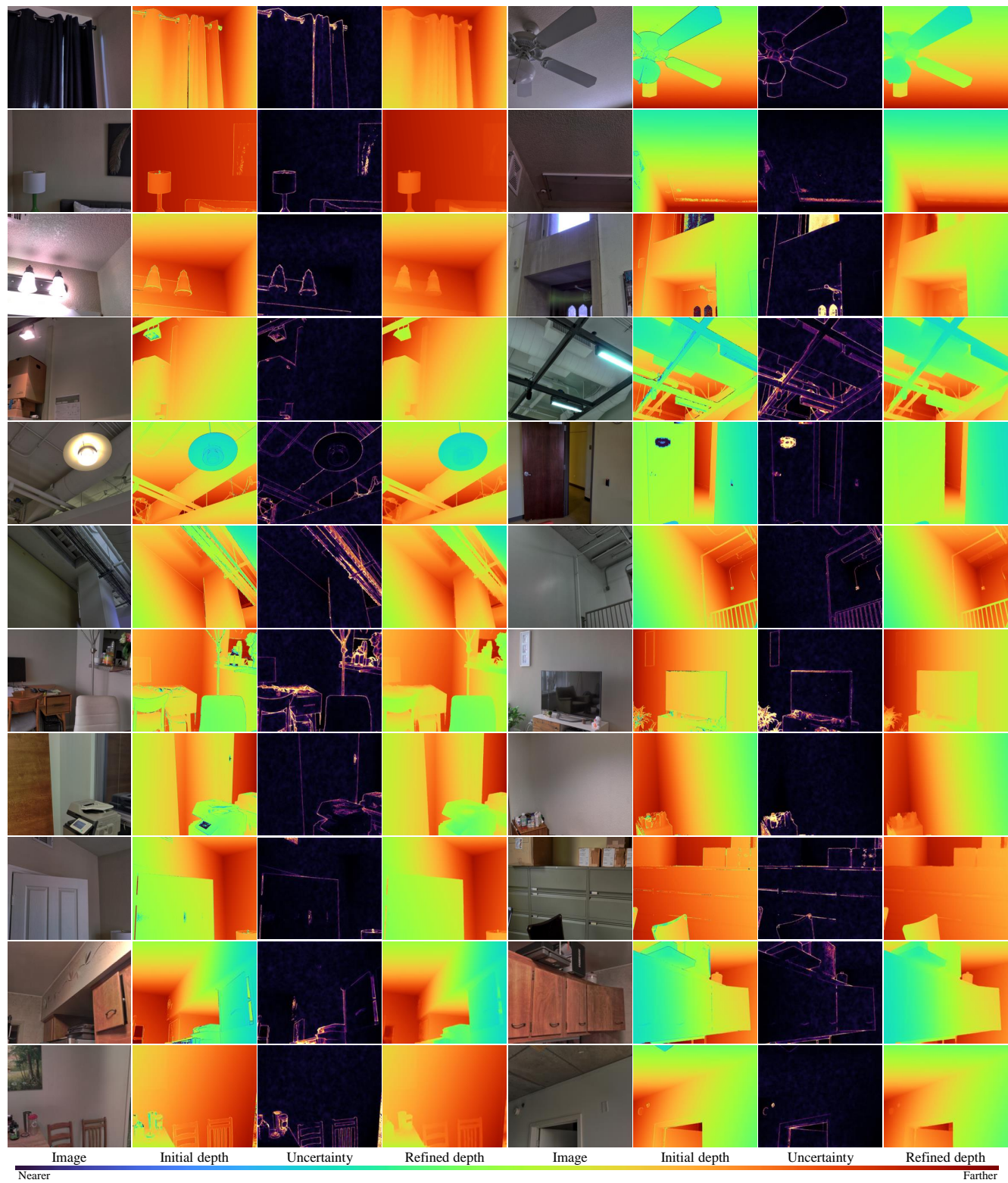


Figure 7. Sensor depth enhancement result on DIODE-Indoor.

D. Noisy depth completion

Fig. 8 and Fig. 9 illustrates the refinement result of noisy depth completion on NYUv2 [55] using CFormer [70] and MSPN [30], respectively.

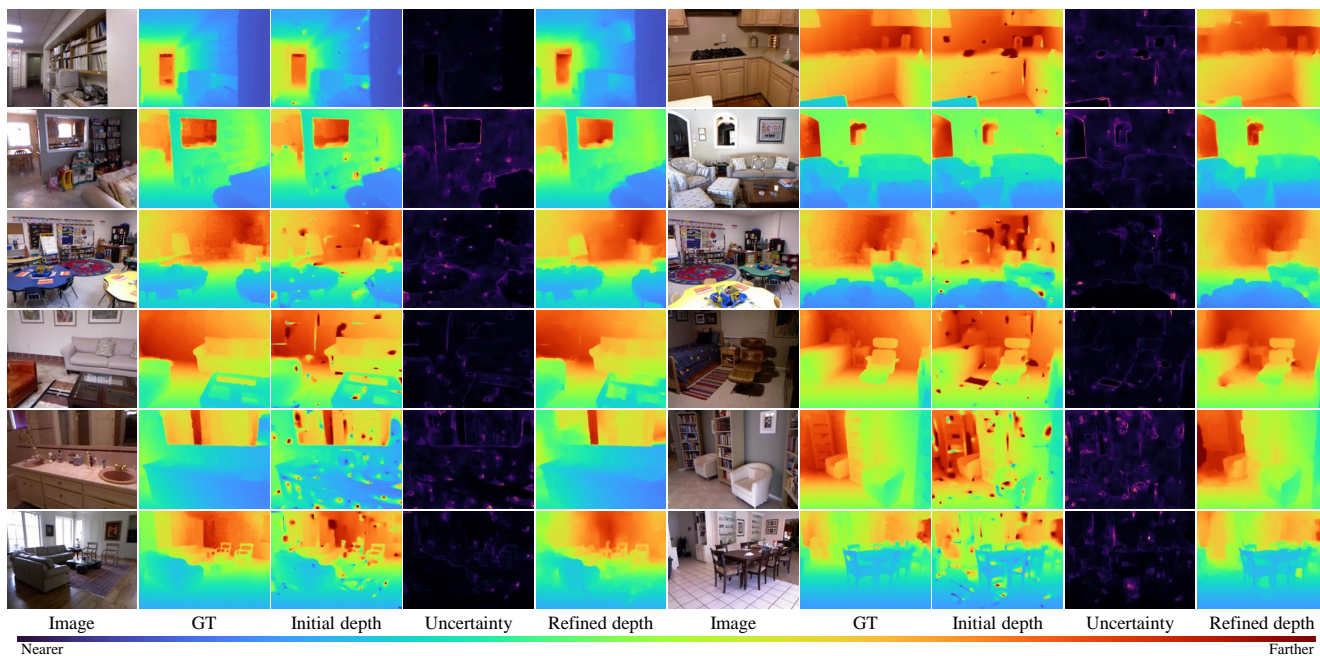


Figure 8. Refinement result on noisy depth completion using CFormer.

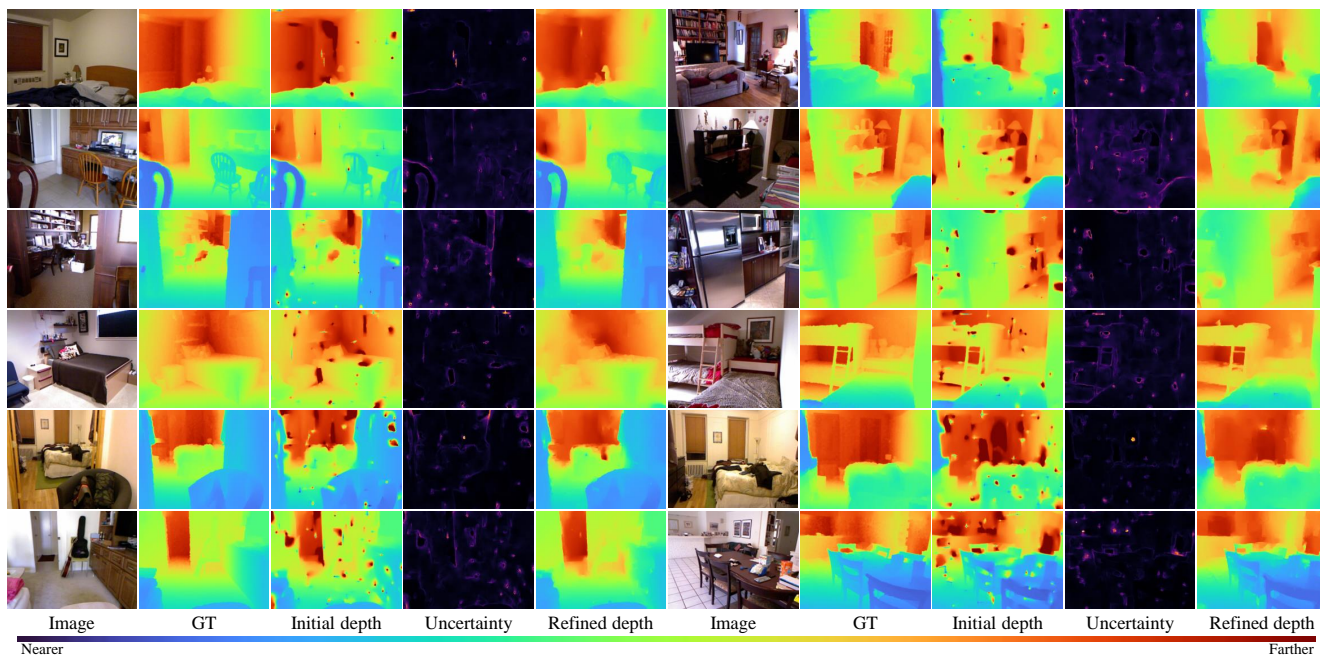


Figure 9. Refinement result on noisy depth completion using MSPN.

E. Depth inpainting

Fig. 10 and Fig. 11 illustrates the depth inpainting result on ScanNet [13] and NYUv2 [55], respectively.

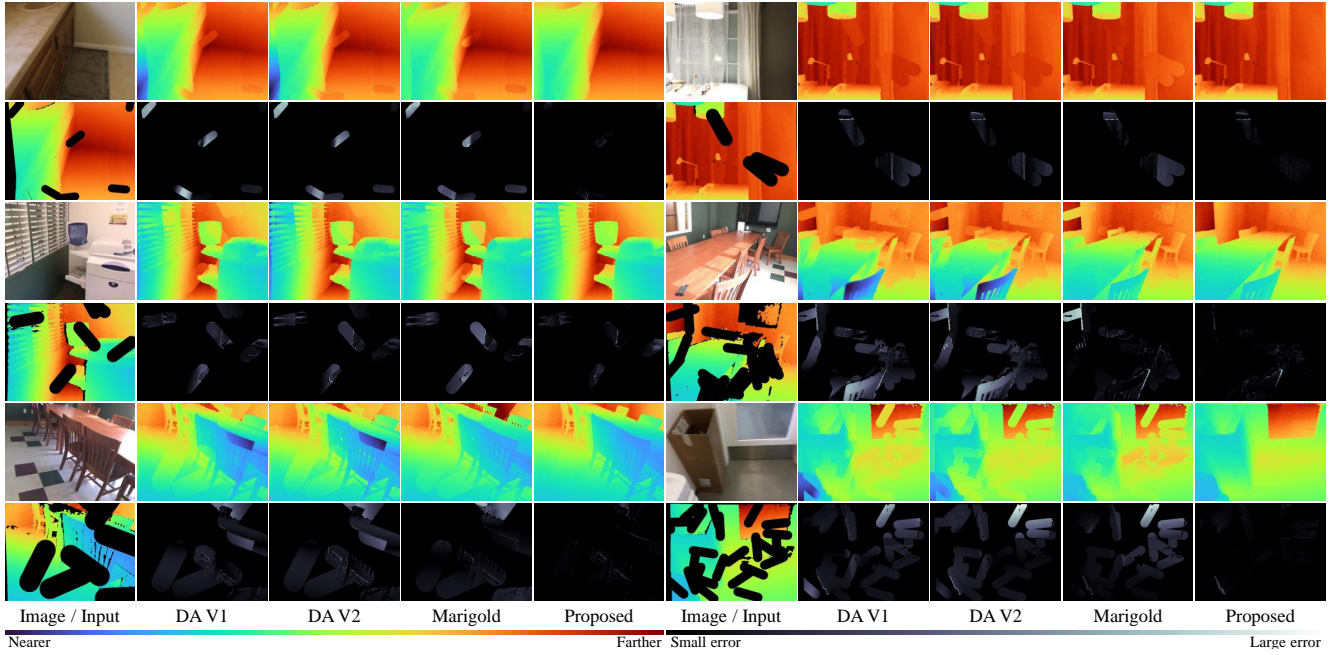


Figure 10. Qualitative comparison of depth inpainting results on ScanNet. For each depth map, the corresponding error map is provided below, in which brighter pixels represent large errors.

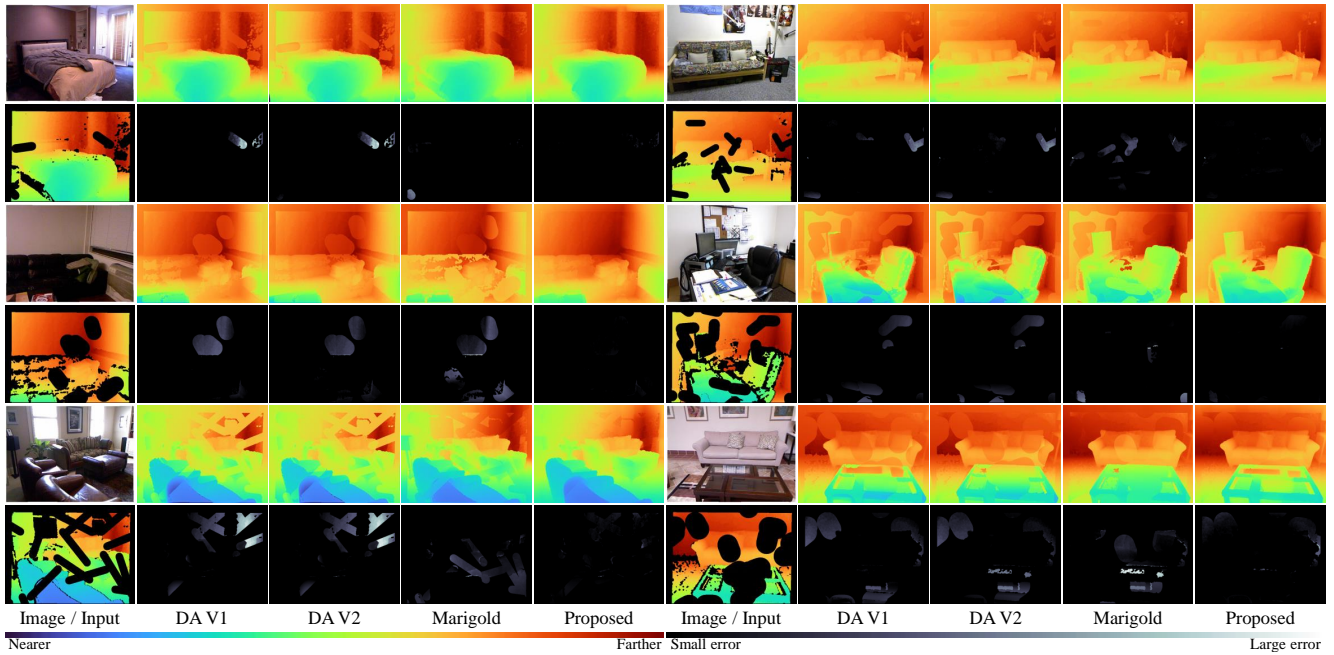


Figure 11. Qualitative comparison of depth inpainting results on NYUv2. For each depth map, the corresponding error map is provided below, in which brighter pixels represent large errors.

F. Ethics statement

This work is conducted as part of a research project. While we plan to share the code and findings to promote transparency and reproducibility in research, we currently have no plans to incorporate this work into a commercial product. In all aspects of this research, we are committed to adhering to Microsoft AI principles, including fairness, transparency, and accountability.